Received: 11 April 2022 | Revised: 26 August 2022 | Accepted: 24 September 2022

DOI: 10.1002/mp.16018

RESEARCH ARTICLE

MEDICAL PHYSICS

Assessment of pulmonary morphometry using hyperpolarized ^{129}Xe diffusion-weighted MRI with variable-sampling-ratio compressed sensing patterns

Qian Zhou[1,2] | **Haidong Li**[1,2] | **Qiuchen Rao**[1] | **Ming Zhang**[1,2] | **Xiuchao Zhao**[1,2] | **Luyang Shen**[1] | **Yuan Fang**[1] | **Hongchuang Li**[1,2] | **Xiaoling Liu**[1,2] | **Sa Xiao**[1,2] | **Lei Shi**[1,2] | **Yeqing Han**[1,2] | **Chaohui Ye**[1,2] | **Xin Zhou**[1,2]

[1]Key Laboratory of Magnetic Resonance in Biological Systems, State Key Laboratory of Magnetic Resonance and Atomic and Molecular Physics, National Center for Magnetic Resonance in Wuhan, Wuhan Institute of Physics and Mathematics, Innovation Academy for Precision Measurement Science and Technology, Chinese Academy of Sciences-Wuhan National Laboratory for Optoelectronics, Wuhan, China

[2]University of Chinese Academy of Sciences, Beijing, China

Correspondence
Xin Zhou, Key Laboratory of Magnetic Resonance in Biological Systems, State Key Laboratory of Magnetic Resonance and Atomic and Molecular Physics, National Center for Magnetic Resonance in Wuhan, Wuhan Institute of Physics and Mathematics, Innovation Academy for Precision Measurement Science and Technology, Chinese Academy of Sciences-Wuhan National Laboratory for Optoelectronics, 30 West Xiaohongshan, Wuhan 430071, China.
Email: xinzhou@wipm.ac.cn

Funding information
National key Research and Development Project of China, Grant/Award Number: 2018YFA0704000; National Natural Science Foundation of China, Grant/Award Numbers: 91859206, 21921004, 11905288, 81871321, 81930049; Scientific Instrument Developing Project of the Chinese Academy of Sciences, Grant/Award Numbers: GJJSTD20200002, YJKYYQ20200067; Key Research Program of Frontier Sciences, CAS, Grant/Award Number: ZDBS-LY-JSC004; Hubei Provincial Key Technology Foundation of China, Grant/Award Number: 2021ACA013; Innovation Project of

Abstract

Background: Hyperpolarized (HP) ^{129}Xe multiple *b*-values diffusion-weighted magnetic resonance imaging (DW-MRI) has been widely used for quantifying pulmonary microstructural morphometry. However, the technique requires long acquisition times, making it hard to apply in patients with severe pulmonary diseases, who cannot sustain long breath holds.

Purpose: To develop and evaluate the technique of variable-sampling-ratio compressed sensing (VCS) patterns for accelerating HP ^{129}Xe multiple *b*-values DW-MRI in humans.

Methods: Optimal variable sampling ratios and corresponding *k*-space undersampling patterns for each *b*-value were obtained by retrospective simulations based on the fully sampled (FS) DW-MRI dataset acquired from six young healthy volunteers. Then, the FS datasets were retrospectively undersampled using both VCS patterns and conventional compressed sensing (CS) pattern with a similar average acceleration factor. The quality of reconstructed images with retrospective VCS (rVCS) and CS (rCS) datasets were quantified using mean absolute error (MAE) and structural similarity (SSIM). Pulmonary morphometric parameters were also evaluated between rVCS and FS datasets. In addition, prospective VCS multiple *b*-values ^{129}Xe DW-MRI datasets were acquired from 14 cigarette smokers and 13 age-matched healthy volunteers. The differences of lung morphological parameters obtained with the proposed method were compared between the groups using independent samples *t*-test. Pearson correlation coefficient was also utilized for evaluating the correlation of the pulmonary physiological parameters obtained with VCS DW-MRI and pulmonary function tests.

Results: Lower MAE and higher SSIM values were found in the reconstructed images with rVCS measurement when compared to those using conventional rCS measurement. The details and quality of the images obtained with rVCS and FS measurements were found to be comparable. The mean values of the morphological parameters derived from rVCS and FS datasets showed no significant differences ($p > 0.05$), and the mean differences of measured acinar duct radius, mean linear intercept, surface-to-volume ratio, and apparent diffusion coefficient with cylinder model were −0.87%, −2.42%, 2.04%, and −0.50%,

Qian Zhou, Haidong Li, and Qiuchen Rao contributed equally to this work.

Optics Valley Laboratory, Grant/Award Numbers: OVL2021ZD003, OVL2021ZD004; Youth Innovation Promotion Association, Grant/Award Numbers: 2020330, 2021330; Tencent Foundation: the Xplorer Prize

respectively. By using the VCS technique, significant differences were delineated between the pulmonary morphometric parameters of healthy volunteers and cigarette smokers ($p < 0.001$), while the acquisition time was reduced by four times.

Conclusion: A fourfold reduction in acquisition time was achieved using the proposed VCS method while preserving good image quality. Our preliminary results demonstrated that the proposed method can be used for evaluating pulmonary injuries caused by cigarette smoking and may prove to be helpful in diagnosing lung diseases in clinical practice.

KEYWORDS
compressed sensing, hyperpolarized ^{129}Xe DW-MRI, variable sampling ratio

1 | INTRODUCTION

Hyperpolarized (HP) ^{129}Xe gas magnetic resonance imaging (MRI) has been regarded as a powerful and noninvasive pulmonary imaging modality due to its ability to quantify regional ventilation,[1–4] microstructure, and gas exchange function of the lungs.[5–8] The potential of this technique in pulmonary disease diagnosis and evaluation has been demonstrated in previous studies.[9–16] Furthermore, the technique of HP ^{129}Xe diffusion-weighted MRI (DW-MRI) is useful in determining the apparent diffusion coefficient (ADC) as well as the alveolar morphological parameters.[17–19] Owing to the sensitivity of these physiological parameters to the alveolar microanatomical changes, they can be used for measuring the changes in pulmonary microstructure caused by lung diseases or aging.[20,21]

Multiple *b*-values gas DW-MRI is one of the widely used noninvasive techniques for assessing pulmonary morphometry.[22,23] Theoretical models of gas diffusion, such as cylinder model (CM)[24] and stretched exponential model[25] allow the measurement of ADC and pulmonary morphometrical parameters, including acinar duct radius (R), mean linear intercept (L_m), and surface-to-volume ratio (SVR), enabling the evaluation the physiological injuries caused by smoking or chronic obstructive pulmonary diseases.[10,20] Data from the multiple *b*-values gas DW-MRI are generally collected within a single breath hold, and the typical acquisition time is more than 15 s. The long acquisition time limits the application of HP multiple *b*-values ^{129}Xe DW-MRI in patients with severe pulmonary diseases, who are unable to sustain long breath holds.

Over the years, rapid improvements in accelerated MRI acquisition techniques have led to a dramatic reduction in acquisition times.[26,27] Among the rapid MRI acquisition methods, compressed sensing (CS) is one of the most convenient and economical methods to speed up MRI acquisition via random undersampling of the *k*-space by using the innate sparsity of MRI data.[28,29] CS has been widely used for accelerating MRI acquisition and improving image resolution because it does not require expensive hardware or complex acquisition schemes.[28–30]

In the previous studies, CS has also been used for accelerating HP gas DW-MRI acquisition and reducing the bias of morphological parameters derived from DW-MR images by improving the signal-to-noise ratio (SNR) of images with larger flip angles.[28,31] Generally, a fixed acceleration factor (AF) was used in these studies.[28] However, with this approach, obvious artifacts caused by *k*-space undersampling acquisition become inevitable when the AF increases, leading to high mean absolute error (MAE) values.[25] Meanwhile, if a fixed AF is used, precise measurement of pulmonary parameters becomes difficult due to signal attenuation.

In this study, the method of variable-sampling-ratio compressed sensing (VCS) patterns was proposed for accelerating HP multiple *b*-values DW-MRI data acquisition while preserving good image reconstruction quality. In the proposed method, different AFs and *k*-space acquisition patterns were utilized, and the AFs were decreased as the *b*-values were increased. The feasibility of this method was demonstrated in both retrospective and prospective experiments. Additionally, pulmonary morphological changes caused by cigarette smoking were also quantified using the proposed method.

2 | MATERIALS AND METHODS

2.1 | Subjects and MR scanner

This study enrolled individuals who had no history of lung diseases. All the human experiments were performed under the approval of the Institutional Review Board. Written informed consent was obtained from each subject prior to research initiation. ^{129}Xe MRI scans were conducted using a 3.0 T human MRI scanner [uMR 780(Xe), verImagin Healthcare, Wuhan, China] with a home-built transmit/receive chest coil, which is

a flexible vest-shaped two-saddle quadrature coil that can wrap around the chest. The coil was tuned to a frequency of 35.49 MHz.

2.2 | ^{129}Xe polarization and delivery

Isotopically enriched xenon gas (86% ^{129}Xe) was polarized using a commercial polarizer system (verImagin Healthcare) via rubidium-vapor spin-exchange optical pumping. HP ^{129}Xe gas was cryogenically accumulated and then thawed into a Tedlar bag. Subsequently, recruited volunteers were requested to inhale 800 ml of a gas mixture composed of 50% xenon and 50% nitrogen from functional residual capacity and hold their breath for ^{129}Xe DW-MRI acquisition. The available spin polarization of xenon gas in the Tedlar bag was approximately 40%.

2.3 | Variable-sampling-ratio compressed sensing patterns

Unlike the conventional CS technique with fixed undersampling pattern or fixed AF, the acquisition strategy put forward in the present study used various AFs and undersampling patterns for DW-MRI data acquisition with different *b*-values. This method relied on the low-rank property of DW-MR images, whose structures are similar and only their signal intensities change with different *b*-values. In addition, it has been previously described that DW-MRI data have sparsity along the *b*-value direction.[32] Therefore, the method of low-rank and sparse (L + S) matrix decomposition was used for image reconstruction.[33] Meanwhile, for obtaining high-quality images and reducing possible artifacts caused by signal attenuation and undersampling, the AF utilized for acquisition was decreased when the *b*-value was increased, that is, more *k*-space data were acquired when a larger *b*-value was applied.

2.3.1 | Fully sampled DW-MRI data acquisition

Fully sampled (FS) ^{129}Xe DW-MRI data were acquired from six healthy volunteers (age: 25.5 ± 1.2 years) for optimizing variable sampling ratios and undersampling *k*-space patterns. Diffusion-weight gradient echo (GRE) sequence was used for data acquisition, and the following acquisition parameters were used: field of view = 380 × 380 mm^2, flip angle = 6°, time of repetition (TR)/time of echo (TE) = 15.5/12.5 ms, matrix size = 64 × 64, number of slices = 4, slice thickness = 30 mm, bandwidth = 600 Hz/pixel, and total acquisition time = 15.9 s. Additionally, diffusion-sensitization gradient was oriented in the slice selection direction, and *b*-values of 0, 10, 20, and 30 s/cm^2 were used with a diffusion time (Δ) of 5 ms (ramp time = 0.3 ms, plateau time = 3.7 ms, gap time between lobes = 0.7 ms). Centric phase encoding order and interleaved acquisition were also used in the data acquisition.[34,35]

2.3.2 | Retrospective VCS simulations

Retrospective simulations were used for obtaining optimal sampling ratios and undersampling patterns for each *b*-value. First, different undersampling patterns were generated using a series of sampling ratios ranging from 0.125 to 0.5 with an interval of 0.025 between each. A pseudo-random variable density undersampling pattern generated by the Monte Carlo method was employed to ensure that the artifacts caused by undersampling were incoherent in the sparse transformation domain.[33,36] The optimal undersampling pattern with the sampling ratio was determined by the transform point spread function with lowest peak interference.[36] Then, FS data were retrospectively undersampled using the generated patterns, followed by CS reconstruction to determine the optimal sampling ratio of each frame. Subsequently, the MAE between the FS and CS images with different sampling ratios was calculated. According to previous literature,[25,31] the quality of the reconstructed images was generally considered acceptable at an MAE of 0.03. Therefore, we chose MAE = 0.03 as the threshold value to determine the optimal sampling ratio.[25,37] The optimal sampling ratio for each *b*-value is the minimum sampling ratio with an MAE of less than 0.03. Subsequently, the final sampling ratios for each *b*-value were obtained by averaging the optimal sampling ratios of each *b*-value across all the six healthy volunteers. Combined with the image quality and the effect of the reconstruction algorithm, the optimal sampling ratios of 0.125, 0.125, 0.325, and 0.45 for *b*-values of 0, 10, 20, and 30 cm^2/s, respectively, were finally determined based on the FS datasets. Thereafter, the optimal *k*-space undersampling patterns were determined by minimizing the MAE between FS images and reconstructed retrospective VCS (rVCS) images. Lastly, we obtained the VCS patterns for multiple *b*-values DW-MRI.

To evaluate the effect of the proposed VCS method, all the FS data from the six young healthy volunteers were retrospectively undersampled using the above VCS patterns. Then, the algorithm of L + S was used to reconstruct the MR images for undersampled VCS data. We define the MR images as I and assume I has two components, that is, the low-rank part (L) and the sparsity part (S) of images, namely:

$$I = L + S \quad (1)$$

Then, we need to obtain the variables in Equation (1) (L and S) by solving the optimization problem described in the following objective function[33]:

$$\min_{L,S} \frac{1}{2} \|T(L+S) - y\|_2^2 + \lambda_L \|L\|_* + \lambda_S \|\psi S\|_1 \quad (2)$$

where T is the operator for encoding or acquisition, L is the low-rank part of images, S is the sparsity part of images, y is the acquired undersampled data, Ψ is the sparse transformation, and the parameters λ_L and λ_S are used to trade-off data consistency versus the complexity of the solution given by the sum of the nuclear and L_1 norms. The optimization problem was solved by using iterative soft thresholding algorithm, and singular values of L and the entries of ΨS were jointly optimized in the algorithm.[33] Based on the empirical values and visual inspection, we used $\lambda_L = 0.01$ and $\lambda_S = 0.01$. After reconstruction, the obtained rVCS images were used for further analysis.

In addition, retrospective simulation using conventional CS with an AF of four was also performed for comparison. The undersampling pattern was generated in the phase-encoding direction as described in previous studies.[35] The Monte-Carlo method was employed with pseudo-random variable density to maximize the incoherence.[33,36] Different undersampling patterns with the AF of four were generated by the transform point spread function with lowest peak interference.[36] The optimal undersampling pattern was determined by minimizing the MAE between FS images and retrospective CS (rCS) reconstructed images.

All the retrospective simulations were performed in-house using the MATLAB software (MathWorks, Natick, MA, USA) software. The quality of reconstructed images was compared with FS images and evaluated using MAE, difference map and structural similarity index (SSIM), which is a measure of the similarity of overall structural information between two images.[38] Moreover, microstructural pulmonary parameters measured via rVCS, including R, L_m, SVR, and ADC, were also compared with the corresponding values obtained using FS datasets. The demographics and pulmonary function tests (PFTs) results are summarized in Table S1.

2.3.3 | Prospective VCS acquisition

Thirteen healthy volunteers without smoking history and 14 cigarette smokers (23.2 ± 13.8 pack-years) were enrolled for the prospective experiments. For prospective VCS acquisition, the accelerated interleaved multi-slice diffusion-weight GRE sequence with centric phase-encoding was used, and the flip angle was set as 8.5°. Due to the VCS patterns, matrix sizes for b-values of 0/10/20/30 s/cm^2 were 64 × (8/8/21/29), respectively. The total acquisition time was 4.1 s, and all the images were reconstructed to a matrix of 64 × 64.

Before DW-MRI data acquisition, PFTs were also performed on each subject, and the parameters including ratio of forced expiratory volume in 1 s to forced vital capacity (FEV_1/FVC) and diffusing capacity of the lung for carbon monoxide as a percentage of the predicted value [DL_{CO} ($\%_{pred}$)] were obtained.

2.4 | Data processing and analysis

All the MRI data were processed using the MATLAB software. For the FS data, the raw data were directly reconstructed into images by applying the fast Fourier transform (FFT). For the rVCS, rCS, and prospective VCS measurements, the undersampled data were reconstructed using the FFT with the algorithm of L + S as described in Section 2.3.2.

By fitting the reconstructed images to the CM model as described previously,[35] pulmonary morphometric parameters such as R, L_m, and SVR were calculated. In addition, ADC map of each subject was also generated by performing a mono-exponential fitting on a pixel-by-pixel basis using the images of $b = 0$ and 10 s/cm^2.

Statistical analysis was performed using the SPSS, version 20.0 (IBM Corp., Armonk, NY, USA). Independent t-test was used to compare the differences of lung morphometry metrics across the groups, and the statistical significance was set at $p < 0.05$ (two tailed). Pearson correlation coefficients were calculated to investigate the correlation between pulmonary morphometric and PFTs parameters.

3 | RESULTS

3.1 | Retrospective VCS results

Figure 1 shows the rCS simulation results for optimal variable sampling ratios from FS datasets in the six healthy volunteers. MAE between the rCS and FS images decreased with an increase in the sampling ratios from 0.125 to 0.5. The pink plane in the figure denotes the MAE threshold of 0.03. For the first two frames ($b = 0$ and 10 s/cm^2), the simulation results showed that the MAEs of all the sampling ratios were less than 0.03, and the minimum of 0.125 was chosen as the optimal sampling ratio. As for the third frame ($b = 20$ s/cm^2), there was a cross between the MAEs and the pink plane (MAE = 0.03) in different volunteers corresponding to different sampling ratios. Thus, the sampling ratio was determined to be 0.325, as it was closest to the average value. The minimum sampling ratio with MAE of less than 0.03 for the fourth frame

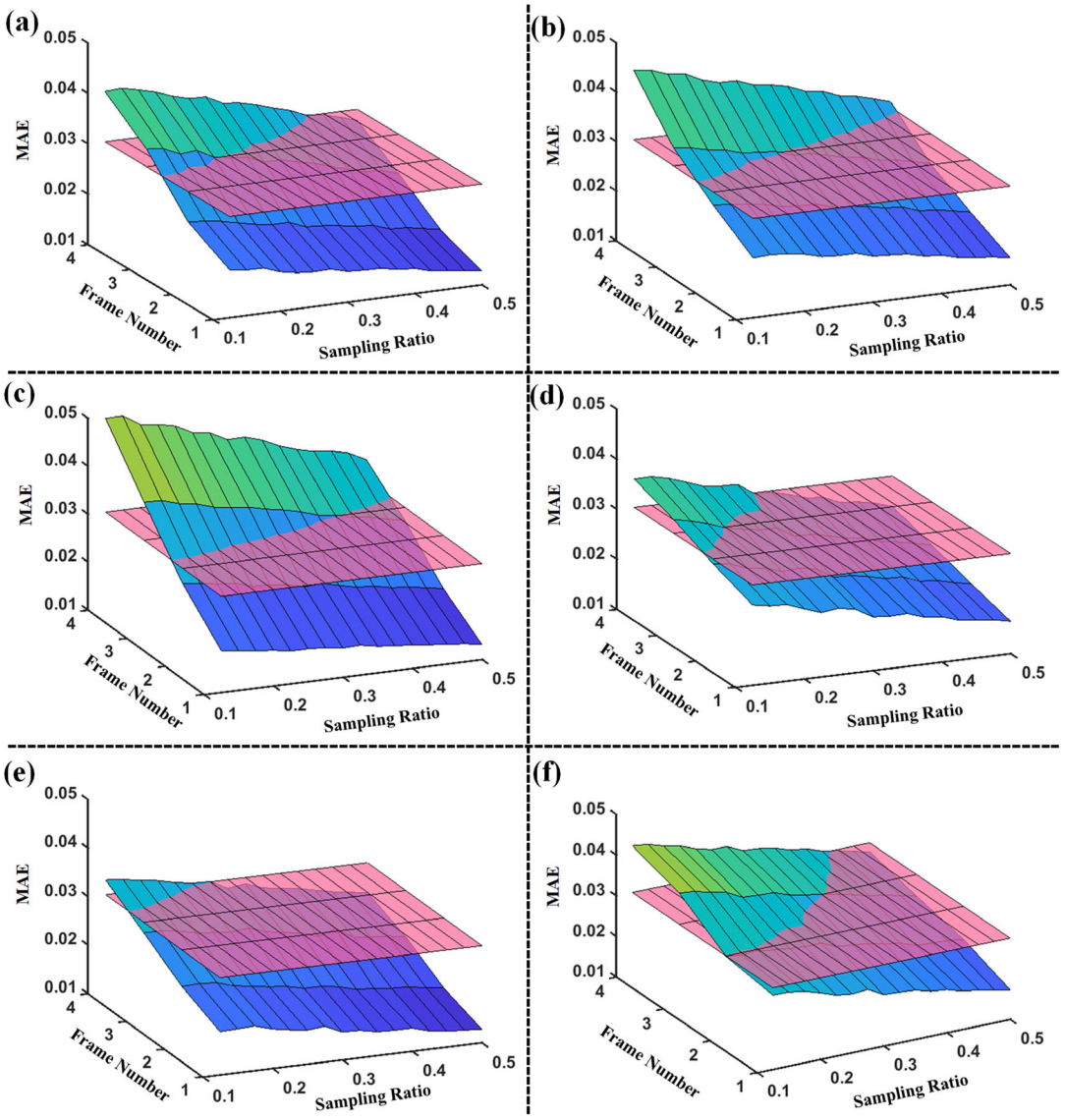

FIGURE 1 The mean absolute error (MAE) values for different sampling ratios with multiple frame numbers (corresponding to *b*-values of 0, 10, 20, 30 s/cm^2) from six healthy volunteers (a–f). The vertical axis is the reconstruction error (MAE) and the pink plane is the threshold of MAE (0.03). Different colors represent different MAEs, ranging from 0.01 to 0.05. MAE varied widely according to the frame number and sampling ratio. With the increase in sampling ratio, the value of MAE decreased.

($b = 30$ s/cm^2) varied among the different datasets, and again, we chose the sampling ratio (0.45) closest to the average as the optimal sampling ratio. To determine the sampling ratio corresponding to MAE of less than 0.03 for the fourth frame, we increased the range of sampling ratio (Figure 1b,c) for two volunteers (as shown in Figure S1). Finally, the optimal variable sampling ratios for the four *b*-values were obtained as 0.125, 0.125, 0.325, 0.45, respectively.

Figure 2a–c shows the representative ^{129}Xe DW-MR images of the healthy volunteer acquired using the strategies of FS, rVCS, and rCS. Obvious signal decay with increased *b*-values could be observed in all acquisition strategies. Figure 2d shows the optimal *k*-space undersampling patterns for variable sampling ratios, and the AFs for each *b*-value were 8, 8, 3.1, and 2.2, respectively. Moreover, the optimal conventional CS undersampling pattern with AF of four is also shown in Figure 2d. The rVCS images had better visual effect than the corresponding rCS images. When compared with original images, images reconstructed with rVCS had lower MAE and higher SSIM than those with rCS. Meanwhile, increased MAE and decreased SSIM could be observed in the images with the larger *b*-values for both the methods. Moreover, the MAEs and SSIMs of rVCS and rCS simulations from six healthy volunteers (the representative slice) are summarized in Table 1.

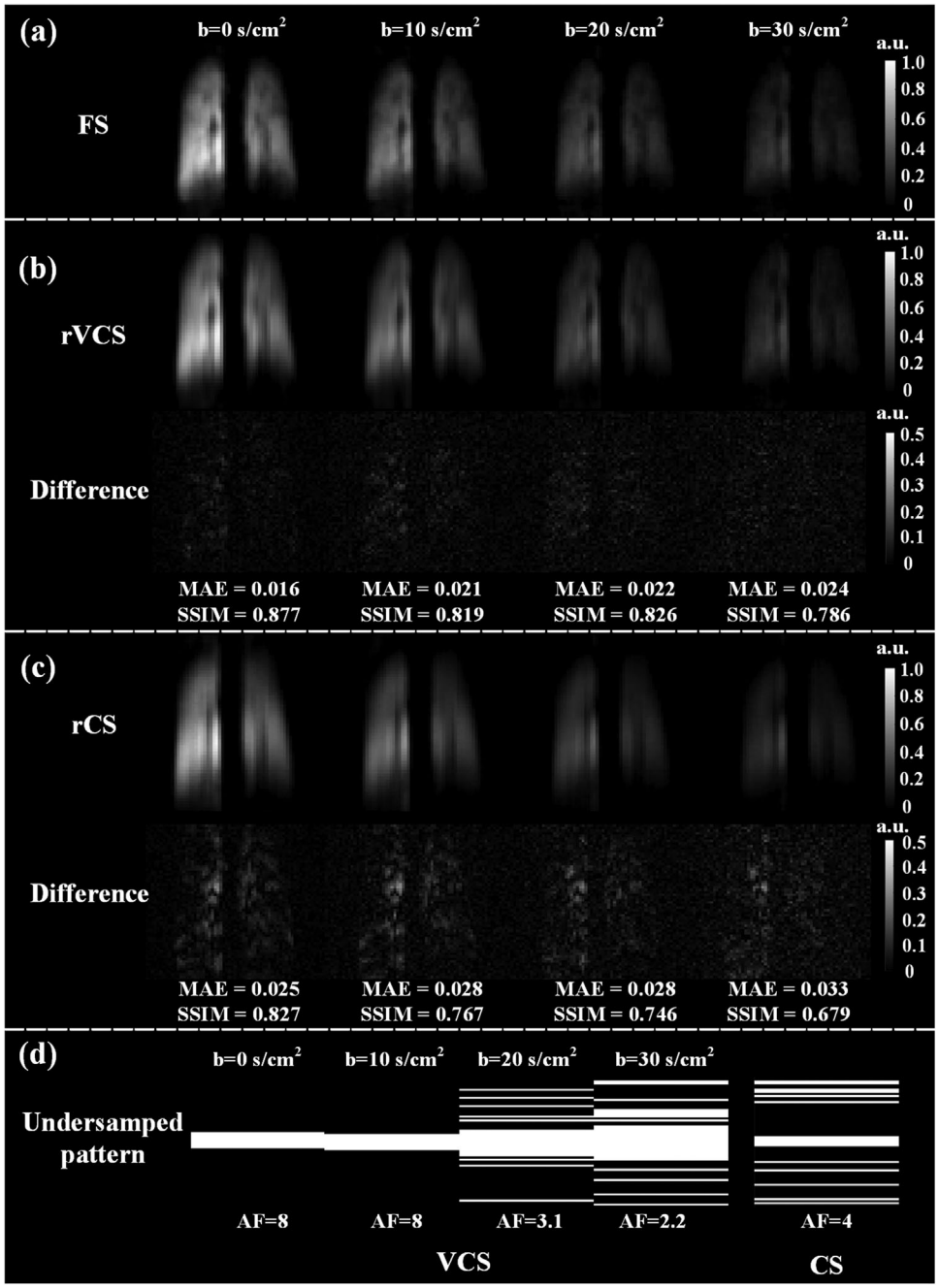

FIGURE 2 Representative results of retrospective variable-sampling-ratio compressed sensing (rVCS) and retrospective compressed sensing (rCS) simulations from the healthy volunteer. (a) Original images, that is, fully sampled (FS) images with *b*-values of 0, 10, 20, and 30 s/cm^2. (b) Reconstructed rVCS images using optimal variable *k*-space undersampling patterns and difference maps compared with original images for each *b*-value. (c) Reconstructed rCS images using optimal fixed *k*-space undersampling pattern and difference maps compared with original images for each *b*-value. Images reconstructed with rVCS had lower mean absolute error (MAE) and higher structural similarity (SSIM) than those with rCS, when compared with the original images. (d) The optimal *k*-space undersampling patterns for VCS and CS data acquisition. The acceleration factors (AFs) of VCS were 8, 8, 3.1, and 2.2, and the AF of conventional CS was 4.

Figure 3 shows the typically measured R, L_m, SVR, and ADC maps of the center slice from a healthy volunteer using FS and rVCS methods. The maps of pulmonary morphometric parameters from rVCS datasets were compared with those generated using FS datasets. The differences of measured R, L_m, SVR, and ADC between FS and rVCS measurements were less than 2%. For the six healthy volunteers, no significant differences were found in the obtained lung microstructural parameters derived from rVCS and FS datasets ($p > 0.05$). Meanwhile, the differences of measured R, L_m, SVR, and ADC between FS and rVCS

TABLE 1 Mean absolute errors (MAEs) and structural similarities (SSIMs) of retrospective variable-sampling-ratio compressed sensing (rVCS) and retrospective compressed sensing (rCS) simulations from the representative slice of six healthy volunteers (HVs)

	MAE (rVCS-FS)					MAE (rCS-FS)				
	$b = 0$ s/cm^2	$b = 10$ s/cm^2	$b = 20$ s/cm^2	$b = 30$ s/cm^2	Mean	$b = 0$ s/cm^2	$b = 10$ s/cm^2	$b = 20$ s/cm^2	$b = 30$ s/cm^2	Mean
HV1	0.016	0.021	0.022	0.024	**0.021**	0.025	0.028	0.028	0.033	**0.029**
HV2	0.018	0.020	0.023	0.023	**0.021**	0.020	0.024	0.027	0.034	**0.026**
HV3	0.016	0.017	0.017	0.020	**0.018**	0.024	0.028	0.029	0.035	**0.029**
HV4	0.019	0.023	0.023	0.027	**0.023**	0.024	0.029	0.033	0.038	**0.031**
HV5	0.022	0.021	0.022	0.021	**0.022**	0.032	0.033	0.034	0.037	**0.034**
HV6	0.015	0.018	0.018	0.019	**0.018**	0.021	0.022	0.025	0.029	**0.024**
	SSIM (rVCS-FS)					**SSIM (rCS-FS)**				
	$b = 0$ s/cm^2	$b = 10$ s/cm^2	$b = 20$ s/cm^2	$b = 30$ s/cm^2	Mean	$b = 0$ s/cm^2	$b = 10$ s/cm^2	$b = 20$ s/cm^2	$b = 30$ s/cm^2	Mean
HV1	0.877	0.819	0.826	0.786	**0.827**	0.826	0.767	0.746	0.679	**0.755**
HV2	0.883	0.834	0.818	0.782	**0.829**	0.868	0.798	0.747	0.690	**0.776**
HV3	0.854	0.819	0.824	0.821	**0.829**	0.822	0.785	0.749	0.706	**0.765**
HV4	0.838	0.756	0.758	0.684	**0.759**	0.831	0.764	0.710	0.619	**0.731**
HV5	0.821	0.780	0.805	0.788	**0.798**	0.791	0.749	0.720	0.677	**0.734**
HV6	0.840	0.789	0.796	0.774	**0.800**	0.813	0.775	0.718	0.678	**0.746**

Note: FS denotes data from fully sampled acquisition.

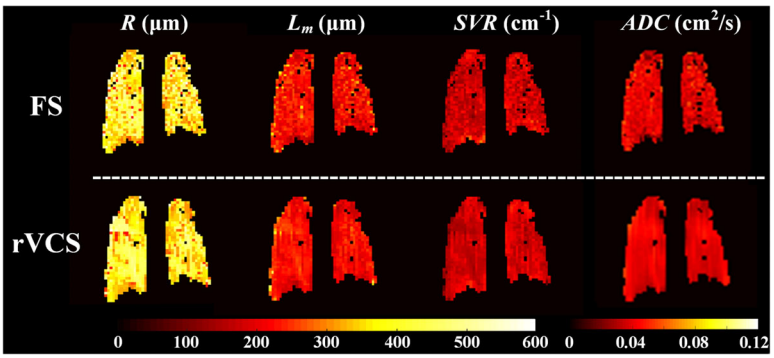

FIGURE 3 Representative pulmonary microstructural parameter maps of the center slice obtained using fully sampled (FS) and retrospective variable-sampling-ratio compressed sensing (rVCS) methods from a healthy volunteer. The measured pulmonary morphometric parameter maps using rVCS agreed with those obtained by FS, and the differences were less than 2%.

acquisition were −0.87%, −2.42%, 2.04%, and −0.50%, with p-values of 0.906, 0.873, 0.818, and 0.963, respectively.

3.2 | Prospective VCS results

Table 2 summarizes the demographics, PFTs, and pulmonary morphometric parameters of healthy and cigarette smoking volunteers in the prospective experiments. The mean ages of the healthy and cigarette smoking volunteers were 48.9 ± 11.2 years and 55.6 ± 7.4 years ($p = 0.075$), respectively. The measured FEV_1/FVC were 79.7 ± 6.6% and 71.7 ± 8.6% for healthy and smoking groups, and significant difference was found between the two groups ($p = 0.012$). Moreover, the measured DL_{CO} ($\%_{pred}$) in the healthy group (95.1 ± 8.8%) was higher ($p = 0.043$) than that in the smoking group (83.6 ± 15.7%). All the morphometric parameters derived from prospective VCS DW-MRI, including R, L_m, SVR, and ADC showed significant differences between the groups ($p < 0.001$). SVR in the cigarette smoking group was found to be lower (160 ± 22 cm^{-1} vs. 207 ± 17 cm^{-1}, $p < 0.001$), while R and L_m were observed to be higher ($p < 0.001$) than those in the healthy group. In addition, the measured mean ADC estimate of smoking group (0.0454 cm^2/s) was obviously higher ($p < 0.001$) than that of the healthy group (0.0351 cm^2/s). The specific results for each subject are summarized in Tables S2 and S3.

Figure 4 shows the DW-MR images obtained from a healthy volunteer and a cigarette smoker using prospective VCS acquisition. The pulmonary structure was preserved in both the healthy individual and the smoker, though some regions were smoothed by reconstruction algorithm. Compared to the healthy volunteer, heterogeneity and small ventilation defect regions could be observed in the lung of the cigarette smoker. Moreover, lower SVR and higher R, L_m, and ADC were found in morphometric parameter maps of the cigarette

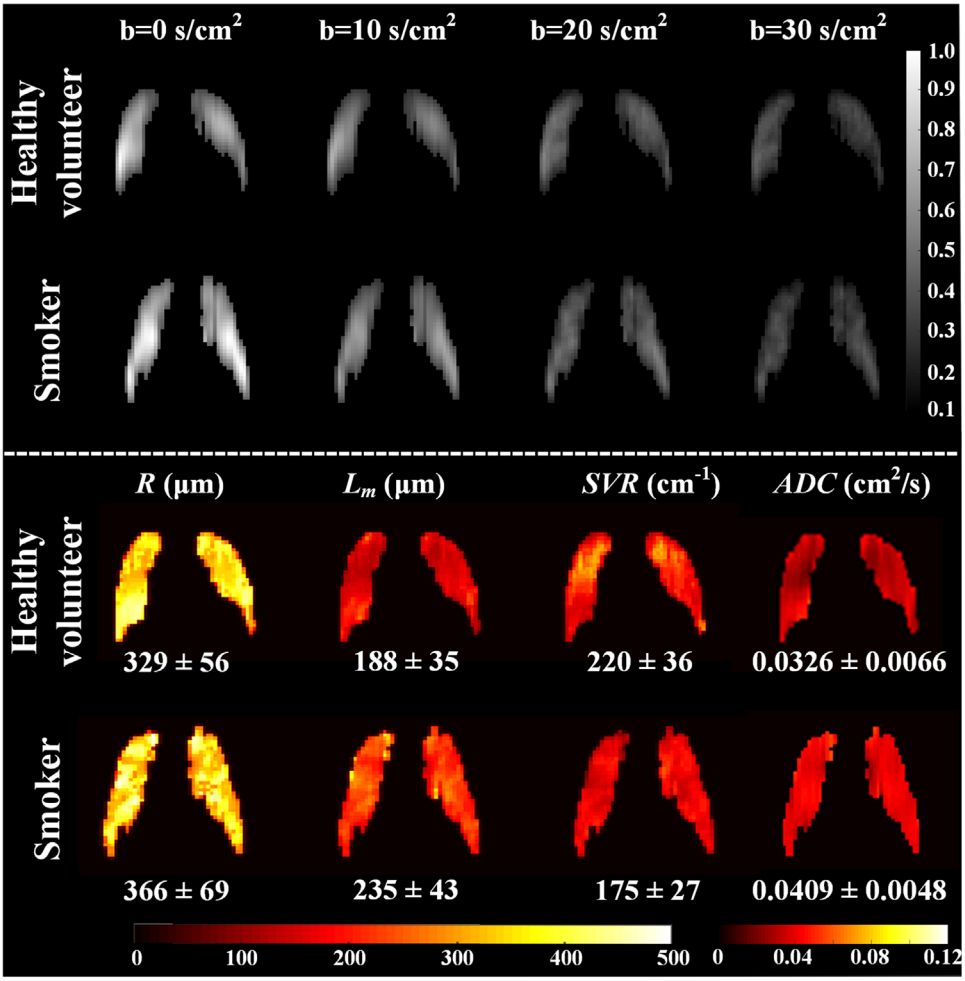

FIGURE 4 Representative ^{129}Xe diffusion-weighted magnetic resonance (DW-MR) lung images and corresponding pulmonary parameter maps obtained from a healthy volunteer and cigarette smoker using variable-sampling-ratio compressed sensing (VCS) method. Typical acinar duct radius (R), mean linear intercept (L_m), surface-to-volume ratio (SVR), and apparent diffusion coefficient (ADC) maps showed significant differences between the healthy volunteer and cigarette smoker.

smoker. Meanwhile, the measured morphometric parameters, including R, L_m, and SVR (see Table 2) showed significant differences ($p < 0.001$) between the groups.

Figure 5 shows the correlation of the measured morphometric parameters using VCS DW-MRI and the parameters measured via the PFTs. The measured R, L_m, SVR, and ADC revealed good correlation with FEV_1/FVC ($r = –0.540, p = 0.004$; $r = –0.566, p = 0.002$; $r = 0.499, p = 0.008$; $r = –0.538, p = 0.004$, respectively). Moreover, good correlations were observed between the measured L_m and DL_{CO} ($\%_{pred}$) ($r = –0.635, p = 0.001$), as well as the ADC and DL_{CO} ($\%_{pred}$) ($r = –0.611$, $p = 0.002$).

4 | DISCUSSION

In this study, a method employing VCS patterns was proposed for accelerating HP ^{129}Xe DW-MRI data acquisition. The optimal undersampling patterns of variable sampling ratios were obtained via retrospective simulations. Additionally, the proposed VCS method was also used for evaluating the pulmonary morphological changes caused by cigarette smoking in prospective study. Both the retrospective and prospective results demonstrated that the proposed VCS approach is capable of achieving comparable image quality and reliable pulmonary microstructural parameters with higher AFs.

Unlike the conventional CS method, the proposed VCS method utilized undersampled patterns with variable sampling ratios for DW-MRI data acquisition. Since only the signal would attenuate when the applied b-value is increased in DW-MRI, the structure of the images would not change, which means that the resulting images have the property of low rank in the dimension of b-values.[37] Considering the fact that higher b-values would cause more attenuation in the images, the strategy of increasing the sampling ratio

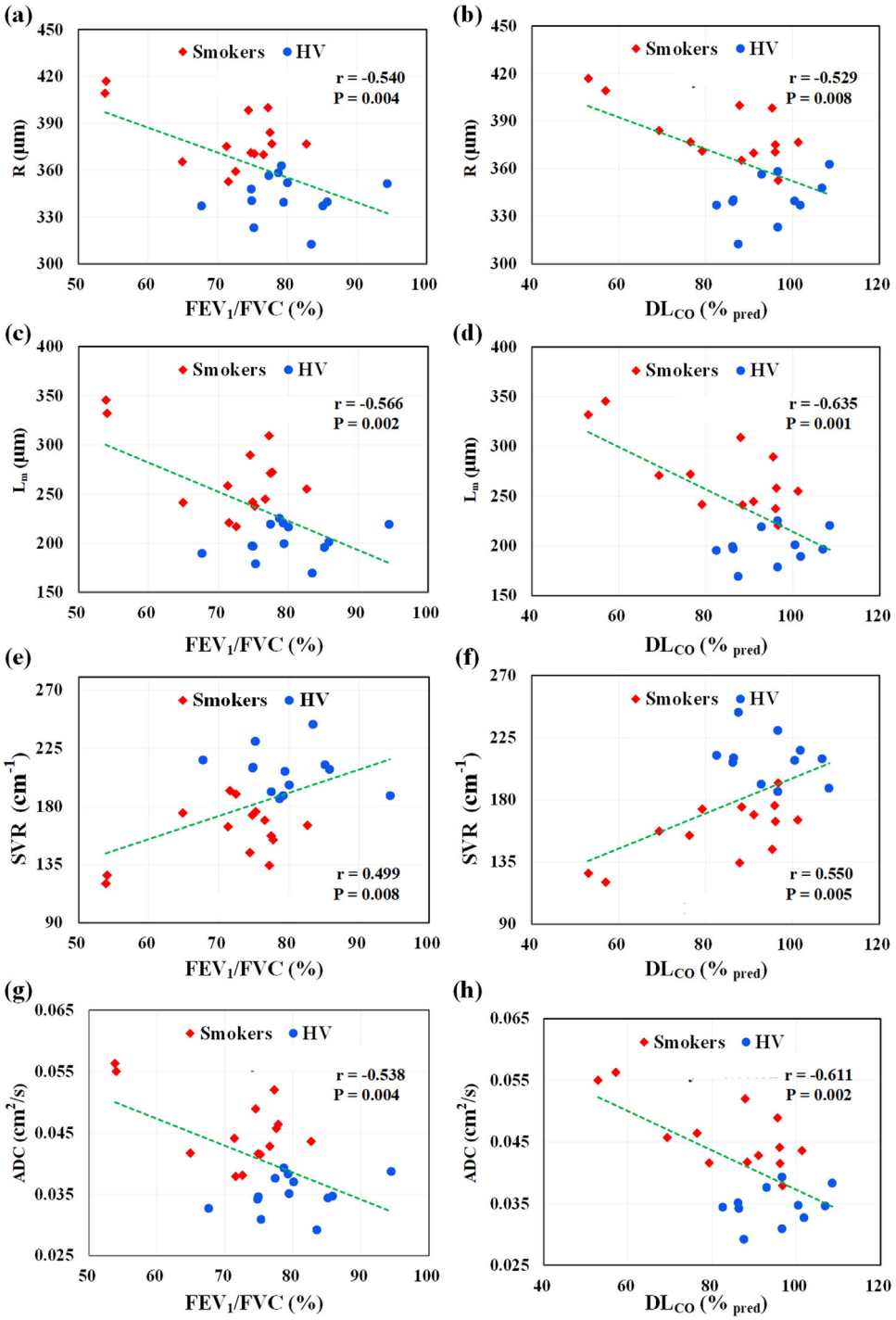

FIGURE 5 (a–h) Correlations of morphometric parameters derived by variable-sampling-ratio compressed sensing (VCS) diffusion-weighted magnetic resonance imaging (DW-MRI) and functional parameters obtained through pulmonary function tests (PFTs) in all subjects. Acinar duct radius (R), mean linear intercept (L_m), and apparent diffusion coefficient (ADC) showed a negative correlation with the ratio of forced expiratory volume in 1 s to forced vital capacity (FEV_1/FVC), while surface-to-volume ratio (SVR) had a positive correlation with FEV_1/FVC. Morphometric parameters including R, L_m, SVR, and ADC also demonstrated a good correlation with the measured diffusing capacity of the lung for carbon monoxide as a percentage of the predicted value [DL_{CO} ($\%_{pred}$)].

for higher *b*-values was utilized to reduce reconstruction errors in the images. For the global sparsity and low-rank effects of the DW-MRI data, L + S algorithm was used in image reconstruction for reducing the image loss caused by undersampling.[33,37]

The optimal sampling ratios for each *b*-value image were determined by averaging the optimal sampling ratios of each *b*-value image across all the six healthy volunteers in the retrospective experiment. Generally, either the minimum or average optimal sampling ratios

TABLE 2 Demographics, pulmonary function tests (PFTs), and prospective variable-sampling-ratio compressed sensing (VCS) diffusion-weighted magnetic resonance imaging (DW-MRI) results of healthy volunteers and cigarette smokers

Parameters, mean ± SD	Healthy volunteers (n = 13)	Cigarette smokers (n = 14)	p-Value[a]
Demographics			
Age (years)	48.9 ± 11.2	55.6 ± 7.4	0.075
Sex (M/F)	2/11	11/3	–
BMI (kg/m^2)	24.4 ± 2.7	22.5 ± 2.7	0.089
PFTs			
FEV_1/FVC (%)	79.7 ± 6.6	71.7 ± 8.6	0.012
DL_{CO} (%$_{pred}$)	95.1 ± 8.8	83.6 ± 15.7	0.043
VCS DW-MRI			
R (μm)	343 ± 14	380 ± 19	<0.001
L_m (μm)	202 ± 17	267 ± 39	<0.001
SVR (cm^{-1})	207 ± 17	160 ± 22	<0.001
ADC (cm^2/s)	0.0351 ± 0.0030	0.0454 ± 0.0058	<0.001

Abbreviations: ADC, apparent diffusion coefficient; BMI, body mass index; DL_{CO}, diffusing capacity of the lung for carbon monoxide; F, female; FEV_1, forced expiratory volume in 1 s; FVC, forced vital capacity; L_m, mean linear intercept; M, male; R, acinar duct radius; SD, standard deviation; SVR, surface-to-volume ratio; %$_{pred}$, percent-predicted.

[a]Results of statistical analysis between healthy volunteers and cigarette smokers using an independent samples t-test (two tailed).

of each b-value image could be used as the final optimal ones, but trade-off between the image quality and the AF should be made in practice. As for using the minimum optimal sampling ratio, the images of all the subjects could meet the criteria that MAE <0.03, but the AFs are relatively smaller. As for using the average optimal sampling ratio, higher AFs could be obtained with the expense of a slight loss in image quality in some subjects. Finally, the average sampling ratios of each b-value image were chosen as the final optimal sampling ratios after comparing the loss of image quality using average sampling ratios (MAE difference is 22.9%, 0.036 vs. 0.0293) and the decrease of AF using the minimum sampling ratios (AF difference is 31.8%, 1.5 vs. 2.2). Additionally, the retrospective and prospective results also showed the feasibility of the average optimal sampling ratios of each b-value image used as the final optimal ones for the pulmonary morphological parameters assessment.

Our results indicated that the suggested method of VCS can obtain better reconstructed image quality compared with the conventional CS technique, when using the same AFs and reconstructed algorithm. The SNR decreased with an increase in b-value for images with FS acquisition as well as rVCS and rCS measurements. Traditionally, the SNR of images obtained via rVCS and rCS techniques is larger than that acquired by FS acquisition, which is due to the denoising process associated with CS reconstruction.[25] Meanwhile, in our study, the means of SNR of images with maximum b-value of 30 s/cm^2 were 16, 23, and 21 for FS, rVCS, and rCS measurements, respectively. The lowest SNR was 13, which met the Rose criteria of SNR = 5 for the lung morphometric estimates,[39,40] and the measured SNRs for each subject are summarized in Table S4. In addition, our retrospective results suggested that the proposed method can achieve comparable image quality (MAE < 0.03)[25] and reliable lung morphological parameters (the differences were less than 3%) with the FS acquisition. Bland–Altman analysis (Figure S2) of rVCS and FS measurements showed that the mean biases of the R, L_m, SVR, and ADC values between the measurements were 0.86%, 2.48%, −1.76%, and 0.70%, respectively. The voxel-by-voxel skew between FS and rVCS measurements was also assessed via quantile–quantile plots (Figure S3), and most of the points lie on or near the line. The slopes for R, L_m, SVR, and ADC values were 0.91, 0.81, 0.82, and 0.72, respectively, which suggests slight systemic deviations. Moreover, the preliminary prospective experimental results showed that the VCS DW-MRI can be used for quantifying the microstructural changes caused by cigarette smoking and also demonstrated the potential for application of this method in evaluation of lung diseases.

The method recommended in the present study was also used for quantifying the pulmonary microstructural changes caused by cigarette smoking. The measured parameters including R, L_m, SVR, and ADC, derived through the proposed VCS method in healthy volunteers and cigarette smokers, were consistent with that reported in the previous studies.[25,41] Compared with the healthy volunteers, obviously higher R and L_m were observed in cigarette smokers, and these results were in agreement with that reported in the previous studies.[19,25] Meanwhile, the significantly lower SVR was also found in the cigarette smokers, just as that reported with ^{3}He DW-MRI previously.[40,41] Moreover, the measured ADC value for the smokers was significantly higher than that in healthy volunteers, which were consistent with previous studies using HP ^{3}He and ^{129}Xe DW-MRI.[17,20,42,43] These measured microstructural parameters changes in cigarette smokers were probably caused by the microstructural enlargement and airflow restriction caused by cigarette smoking.[17,25,40,42–44]

The goal of this proof-of-concept study was to investigate the feasibility and potential of VCS in HP ^{129}Xe multiple b-values DW-MRI. This study had several limitations. First, the optimal VCS were obtained using L + S algorithm in this study, and new reconstruction techniques such as deep learning[23,45] should be considered in the future studies for increasing the AFs and reducing the possible lost details. Second, the feasibility of the VCS method was demonstrated

in multi-slice two-dimensional sequence. In subsequent studies, three-dimensional diffusion acquisition sequence should be included, which might make it more suitable for random *k*-space sampling. Third, there was a gender mismatch in this study. Although previous studies with limited number of subjects have shown that measured morphological parameters with HP ^{3}He MRI[46] and airspace wall surface area per unit volume of lung tissue with histology[47] are not statistically significant between the genders, more subjects should be enrolled for completely investigating the influence of gender on the measured morphological parameters with gas DW-MRI. Moreover, a fixed dose was used for all the subjects in this study just as reported in the previous studies.[19,25] The expansion would be slightly different between the genders because females have relatively smaller lung volume than males, and adjusted doses according to the lung volume for each subject should be considered in the further studies. In addition, future studies including more subjects with a variety of pulmonary diseases should be conducted for demonstrating the general feasibility of the proposed method.

5 | CONCLUSION

In this study, a method, named VCS patterns, was proposed for accelerating multiple *b*-values DW-MRI. The proposed method was able to accelerate the acquisition speed by four times while preserving good image quality. Our preliminary results demonstrated that this method can be used for evaluating pulmonary injuries caused by cigarette smoking, especially in patients who are unable to hold their breath for a long time.

ACKNOWLEDGMENTS

This work is supported by National key Research and Development Project of China (grant no. 2018YFA0704000), National Natural Science Foundation of China (grant nos. 91859206, 21921004, 11905288, 81871321, 81930049), Scientific Instrument Developing Project of the Chinese Academy of Sciences (grant nos. GJJSTD20200002, YJKYYQ20200067), Key Research Program of Frontier Sciences, CAS (grant no. ZDBS-LY-JSC004), Hubei Provincial Key Technology Foundation of China (2021ACA013), and the Innovation Project of Optics Valley Laboratory (grant nos. OVL2021ZD003, OVL2021ZD004). Haidong Li and Xiuchao Zhao acknowledge the support from Youth Innovation Promotion Association, CAS (grant nos. 2020330, 2021330). Xin Zhou acknowledges the support from the Tencent Foundation through the XPLORER PRIZE.

CONFLICT OF INTEREST

The authors declare they have no conflicts of interest.

DATA AVAILABILITY STATEMENT

The data supporting the findings of this study are available within the article and its Supporting Information.

REFERENCES

1. He M, Driehuys B, Que LG, et al. Using hyperpolarized ^{129}Xe MRI to quantify the pulmonary ventilation distribution. *Acad Radiol*. 2016;23:1521-1531.
2. Svenningsen S, McIntosh M, Ouriadov A, et al. Reproducibility of hyperpolarized ^{129}Xe MRI ventilation defect percent in severe asthma to evaluate clinical trial feasibility. *Acad Radiol*. 2021;28:817-826.
3. Ebner L, Virgincar RS, He M, et al. Multireader determination of clinically significant obstruction using hyperpolarized ^{129}Xe-ventilation MRI. *Am J Roentgenol*. 2019;212:758-765.
4. Niedbalski PJ, Hall CS, Castro M, et al. Protocols for multi-site trials using hyperpolarized ^{129}Xe MRI for imaging of ventilation, alveolar-airspace size, and gas exchange: a position paper from the ^{129}Xe MRI clinical trials consortium. *Magn Reson Med*. 2021;86:2966-2986.
5. Zanette B, Stirrat E, Jelveh S, et al. Physiological gas exchange mapping of hyperpolarized ^{129}Xe using spiral-IDEAL and MOXE in a model of regional radiation-induced lung injury. *Med Phys*. 2018;45:803-816.
6. Zanette B, Santyr G. Accelerated interleaved spiral-IDEAL imaging of hyperpolarized ^{129}Xe for parametric gas exchange mapping in humans. *Magn Reson Med*. 2019;82:1113-1119.
7. Bier EA, Robertson SH, Schrank GM, et al. A protocol for quantifying cardiogenic oscillations in dynamic ^{129}Xe gas exchange spectroscopy: the effects of idiopathic pulmonary fibrosis. *NMR Biomed*. 2019;32:e4029.
8. Collier GJ, Eaden JA, Hughes PJC, et al. Dissolved ^{129}Xe lung MRI with four-echo 3D radial spectroscopic imaging: quantification of regional gas transfer in idiopathic pulmonary fibrosis. *Magn Reson Med*. 2021;85:2622-2633.
9. Li H, Zhao X, Wang Y, et al. Damaged lung gas exchange function of discharged COVID-19 patients detected by hyperpolarized ^{129}Xe MRI. *Sci Adv*. 2021;7:eabc8180.
10. Ruppert K, Qing K, Patrie JT, et al. Using hyperpolarized xenon-129 MRI to quantify early-stage lung disease in smokers. *Acad Radiol*. 2019;26:355-366.
11. Mammarappallil JG, Rankine L, Wild JM, et al. New developments in imaging idiopathic pulmonary fibrosis with hyperpolarized xenon magnetic resonance imaging. *J Thorac Imaging*. 2019;34:136-150.
12. Thomen RP, Walkup LL, Roach DJ, et al. Regional structure-function in cystic fibrosis lung disease using hyperpolarized ^{129}Xe and ultrashort echo magnetic resonance imaging. *Am J Respir Crit Care Med*. 2020;202:290-292.
13. Kaushik SS, Robertson SH, Freeman MS, et al. Single-breath clinical imaging of hyperpolarized ^{129}Xe in the airspaces, barrier, and red blood cells using an interleaved 3D radial 1-point Dixon acquisition. *Magn Reson Med*. 2016;75:1434-1443.
14. Svenningsen S, Nair P, Eddy RL, et al. Bronchial thermoplasty guided by hyperpolarised gas magnetic resonance imaging in adults with severe asthma: a 1-year pilot randomised trial. *ERJ Open Res*. 2021;7:00268-02021.
15. Grist JT, Chen M, Collier GJ, et al. Hyperpolarized ^{129}Xe MRI abnormalities in dyspneic patients 3 months after COVID-19 pneumonia: preliminary results. *Radiology*. 2021;301:E353-E360.
16. Mata J, Guan S, Qing K, et al. Evaluation of regional lung function in pulmonary fibrosis with xenon-129 MRI. *Tomography*. 2021;7:452-465.
17. Stewart NJ, Chan HF, Hughes PJC, et al. Comparison of ^{3}He and ^{129}Xe MRI for evaluation of lung microstructure and ventilation at 1.5T. *J Magn Reson Imaging*. 2018;48:632-642.

18. Ouriadov A, Farag A, Kirby M, et al. Lung morphometry using hyperpolarized ^{129}Xe apparent diffusion coefficient anisotropy in chronic obstructive pulmonary disease. *Magn Reson Med*. 2013;70:1699-1706.
19. Chan HF, Collier GJ, Weatherley ND, et al. Comparison of in vivo lung morphometry models from 3D multiple *b*-value ^{3}He and ^{129}Xe diffusion-weighted MRI. *Magn Reson Med*. 2019;81:2959-2971.
20. Kaushik SS, Cleveland ZI, Cofer GP, et al. Diffusion-weighted hyperpolarized ^{129}Xe MRI in healthy volunteers and subjects with chronic obstructive pulmonary disease. *Magn Reson Med*. 2011;65:1154-1165.
21. Bdaiwi AS, Niedbalski PJ, Hossain MM, et al. Improving hyperpolarized ^{129}Xe ADC mapping in pediatric and adult lungs with uncertainty propagation. *NMR Biomed*. 2022;35:e4639.
22. Chan HF, Weatherley ND, Johns CS, et al. Airway microstructure in idiopathic pulmonary fibrosis: assessment at hyperpolarized ^{3}He diffusion-weighted MRI. *Radiology*. 2019;291:223-229.
23. Duan C, Deng H, Xiao S, et al. Accelerate gas diffusion-weighted MRI for lung morphometry with deep learning. *Eur Radiol*. 2022;32:702-713.
24. Sukstanskii AL, Yablonskiy DA. Lung morphometry with hyperpolarized ^{129}Xe: theoretical background. *Magn Reson Med*. 2012;67:856-866.
25. Chan HF, Stewart NJ, Norquay G, et al. 3D diffusion-weighted ^{129}Xe MRI for whole lung morphometry. *Magn Reson Med*. 2018;79:2986-2995.
26. Lee RF, Johnson G, Grossman RI, et al. Advantages of parallel imaging in conjunction with hyperpolarized helium: a new approach to MRI of the lung. *Magn Reson Med*. 2006;55:1132-1141.
27. Chang YV, Quirk JD, Yablonskiy DA. In vivo lung morphometry with accelerated hyperpolarized ^{3}He diffusion MRI: a preliminary study. *Magn Reson Med*. 2015;73:1609-1614.
28. Ouriadov A, Guo FM, McCormack DG, et al. Accelerated ^{129}Xe MRI morphometry of terminal airspace enlargement: feasibility in volunteers and those with alpha-1 antitrypsin deficiency. *Magn Reson Med*. 2020;84:416-426.
29. Ajraoui S, Parra-Robles J, Wild JM. Incorporation of prior knowledge in compressed sensing for faster acquisition of hyperpolarized gas images. *Magn Reson Med*. 2013;69:360-369.
30. Xiao S, Deng H, Duan C, et al. Considering low-rank, sparse and gas-inflow effects constraints for accelerated pulmonary dynamic hyperpolarized ^{129}Xe MRI. *J Magn Reson*. 2018;290:29-37.
31. Chan H-F, Stewart NJ, Parra-Robles J, et al. Whole lung morphometry with 3D multiple *b*-value hyperpolarized gas MRI and compressed sensing. *Magn Reson Med*. 2017;77:1916-1925.
32. Abascal J, Desco M, Parra-Robles J. Incorporation of prior knowledge of signal behavior into the reconstruction to accelerate the acquisition of diffusion MRI data. *IEEE Trans Med Imaging*. 2018;37:547-556.
33. Otazo R, Candes E, Sodickson DK. Low-rank plus sparse matrix decomposition for accelerated dynamic MRI with separation of background and dynamic components. *Magn Reson Med*. 2015;73:1125-1136.
34. Xie J, Li H, Zhang H, et al. Single breath-hold measurement of pulmonary gas exchange and diffusion in humans with hyperpolarized ^{129}Xe MR. *NMR Biomed*. 2019;32:e4068.
35. Zhang H, Xie J, Xiao S, et al. Lung morphometry using hyperpolarized ^{129}Xe multi-b diffusion MRI with compressed sensing in healthy subjects and patients with COPD. *Med Phys*. 2018;45:3097-3108.
36. Lustig M, Donoho D, Pauly JM, Sparse MRI. The application of compressed sensing for rapid MR imaging. *Magn Reson Med*. 2007;58:1182-1195.
37. Xiao S, Deng H, Duan C, et al. Highly and adaptively undersampling pattern for pulmonary hyperpolarized ^{129}Xe dynamic MRI. *IEEE Trans Med Imaging*. 2019;38:1240-1250.
38. Wang Z, Bovik AC, Sheikh HR, et al. Image quality assessment: from error visibility to structural similarity. *IEEE Trans Image Process*. 2004;13:600-612.
39. Westcott A, Guo F, Parraga G, et al. Rapid single-breath hyperpolarized noble gas MRI-based biomarkers of airspace enlargement. *J Magn Reson Imaging*. 2019;49:1713-1722.
40. Paulin GA, Ouriadov A, Lessard E, et al. Noninvasive quantification of alveolar morphometry in elderly never-and ex-smokers. *Physiol Rep*. 2015;3:e12583.
41. Ouriadov A, Lessard E, Sheikh K, et al. Pulmonary MRI morphometry modeling of airspace enlargement in chronic obstructive pulmonary disease and alpha-1 antitrypsin deficiency. *Magn Reson Med*. 2018;79:439-448.
42. Swift AJ, Wild JM, Fichele S, et al. Emphysematous changes and normal variation in smokers and COPD patients using diffusion ^{3}He MRI. *Eur J Radiol*. 2005;54:352-358.
43. Fain SB, Panth SR, Evans MD, et al. Early emphysematous changes in asymptomatic smokers: detection with ^{3}He MR imaging. *Radiology*. 2006;239:875-883.
44. Quirk JD, Lutey BA, Gierada DS, et al. In vivo detection of acinar microstructural changes in early emphysema with ^{3}He lung morphometry. *Radiology*. 2011;260:866-874.
45. Duan C, Deng H, Xiao S, et al. Fast and accurate reconstruction of human lung gas MRI with deep learning. *Magn Reson Med*. 2019;82:2273-2285.
46. Quirk JD, Sukstanskii AL, Woods JC, et al. Experimental evidence of age-related adaptive changes in human acinar airways. *J Appl Physiol*. 2016;120:159-165.
47. Gillooly M, Lamb D. Airspace size in lungs of lifelong non-smokers: effect of age and sex. *Thorax*. 1993;48:39-43.

SUPPORTING INFORMATION

Additional supporting information can be found online in the Supporting Information section at the end of this article.

How to cite this article: Zhou Q, Li H, Rao Q, et al. Assessment of pulmonary morphometry using hyperpolarized ^{129}Xe diffusion-weighted MRI with variable-sampling-ratio compressed sensing patterns. *Med Phys*. 2023;50:867–878. https://doi.org/10.1002/mp.16018